Materials Research Proceedings 41 (2024) 1887-1896 https://doi.org/10.21741/9781644903131-209

Using the particle finite element method for predicting optimum shear cutting clearance

SANDIN Olle[1,a *], LAROUR Patrick[2,b], RODRÍGUEZ Juan Manuel[1,3,c], KAJBERG Jörgen[1,d] and CASELLAS Daniel[1,4,e]

[1]Department of Engineering Sciences and Mathematics, Division of Solid Mechanics, Luleå University of Technology, Luleå, 971 87, Sweden

[2]Voestalpine Stahl GmbH, voestalpine-Straße 3, Linz, A-4020, Austria

[3]School of Applied Sciences and Engineering, EAFIT University, Medellin, Colombia

[4]Unit of Metallic and Ceramic Materials, Eurecat, Centre Tecnològic de Catalunya, Placa de la Ciència, 2, Manresa, 08243, Spain

[a]olle.sandin@ltu.se, [b]patrick.larour@voestalpine.com, [c]jmrodrigup@eafit.edu.co, [d]jorgen.kajberg@ltu.se, [e]daniel.casellas@eurecat.org

Keywords: Shear Cutting, AHSS, PFEM

Abstract. The shear cutting process, which is the most common cutting technique in the sheet forming industry, is known for introducing damage to the cut edges of high strength metal. This damage may impair the forming- or fatigue properties of the material and can cause edge-cracking during forming or in-service part failure. The edge formability of a sheared edge is strongly linked with the appearance of large notches arising due to unfavorable process parameters. By numerical modelling of the shear cutting process with the possibility to vary important process parameters, the sheared edge damage can be detected and avoided in the manufacturing process. This work present numerical modelling of shear cutting in Advanced High Strength Steel using a novel Particle Finite Element Method approach. Numerical modelling of shear cutting processes over a large range of cutting clearances were conducted and validated against laboratory experiment results. The results showed that the PFEM modelling could detect the cut edge damages with the largest negative impact on formability, thus narrowing the feasible cutting clearance range.

Introduction

The shear cutting process is a common cutting technique in the sheet metal forming industry due to its cost-effectiveness and automation possibilities. However, the shear cutting process is known for inducing damage to the sheared edges that affect the formability and fatigue properties, especially for high strength metal sheets. Such damages may appear as micro-cracks, notches and residual stresses and are shown to be the driving cause of edge-cracking [1–5] and reduced fatigue life [6–11]. Larour et al. [12] showed that sharp geometrical notches such as secondary burnish, excessive burr or rough fracture surfaces have a strong negative influence on the sheared edge formability. The appearance of such geometrical defects is controlled by the cutting clearance, which accordingly is considered an influential cutting process parameter with regards to edge formability. Numerical modelling of the shear cutting process can furthermore be an efficient tool for predicting defects along the cut edge, enabling cutting process optimization, and preventing edge-cracking. However, numerical modelling of shear cutting requires robust numerical handling of large material deformation, which is challenging using conventional Finite Element Methods as element distortion during excessive deformation impair the numerical accuracy. Therefore, the Particle Finite Element Model (PFEM) is applied in this work for the numerical modelling of the shear cutting process, as it efficiently handles the large deformation involved in cutting processes [13–16]. In this work, an axisymmetric PFEM formulation is used for modelling of hole punching

processes that predicts the cut edge morphologies over a large range of cutting clearances. By numerically predicting the appearance of secondary burnish and burr, the model determines the feasible cutting clearance range for a complex-phase AHSS grade of 1.5 mm thickness. The experimental work used for validation of the numerical modelling was presented by Larour et al. [12] and gives the average cut edge zone distribution of punched holes for varying cutting clearances and the corresponding hole expansion ratio (HER) that describes the formability of the punched hole. By predicting the experimental cut edge shapes, including notches such as burr or secondary burnish, and the clear trend between cut edge shape and experimental HER values state the applicability of the PFEM model as an effective tool for predicting the optimum range of cutting clearances for the studied AHSS grade.

The Particle Finite Element Method

PFEM was originally developed by Idelsohn et al. [17] for modelling of incompressible free-flowing surfaces and fluid structure interactions. However, its efficiency in large material deformation and predicting new boundaries makes it suitable for non-linear solid mechanics. This was shown by Rodiguez et al. [15,18–21] for modelling of orthogonal cutting using thermo-mechanical material modelling. Similarly, Oñate et al. [16] showcased numerous examples of non-linear solid mechanics application for PFEM. A recent publication by Sandin et al. [13] applies PFEM for shear cutting of AHSS, where the accuracy and robustness of PFEM for this process is highlighted.

Even though PFEM can be applied on various mechanical problems, the following modelling steps are fundamental [22]:

- Define a volume with a particle distribution.
- Connect the particles using Delaunay triangulation.
- Solve the governing equations using a Lagrangian framework.
- Perform re-connectivity of the particles continuously to prevent element distortion. Transfer results variables.
- The α-shape method, or *constrained* α-shape method [23] as in this work, defines the internal and external boundaries.

Fig. 1 shows the schematic steps of PFEM in a shear cutting context from initial configuration and over a set of time steps.

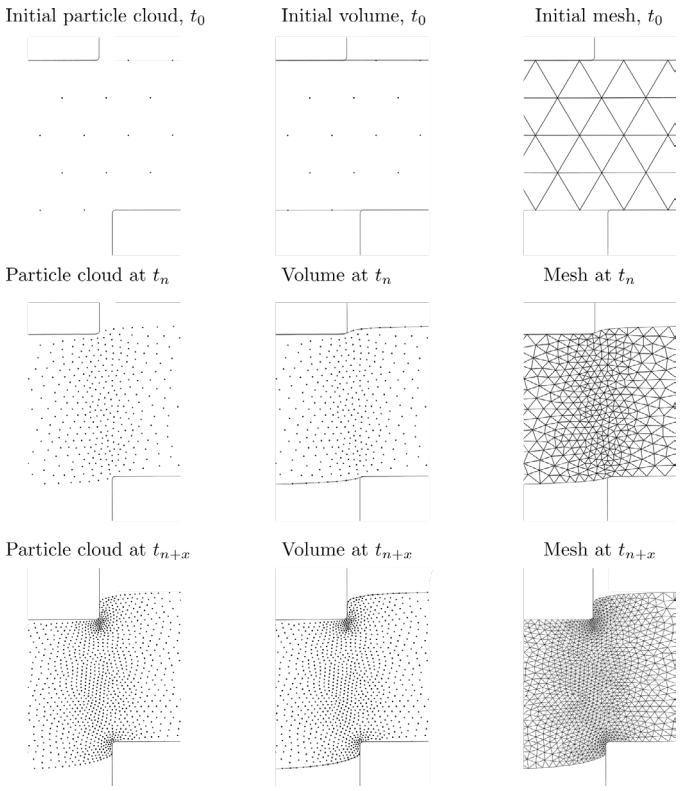

Fig. 1: Schematic steps of the PFEM procedure for shear cutting. Starting from initial time step $\boldsymbol{t_0}$ *to time step* $\boldsymbol{t_{n+x}}$.

The benefits of using PFEM in large deformation solid mechanics are discussed in [13], which in short describes the efficient re-meshing algorithm and computational robustness in large deformations as the main advantages over the conventional Finite Element Method. Meanwhile, the computational efficiency of PFEM is an advantage when comparing it to various mesh-less or particle methods that are developed for large deformation mechanical analysis. The PFEM scheme can insert particles in localized areas for increasing accuracy and can remove particles in redundant areas for reducing the computational cost. However, such operations should be done sparingly as extensive introduction or removal of particles may cause results smoothing or diffusion. Therefore, a fine initial discretization of the problem is suggested.

Constitutive modelling

This work investigates a Complex Phase steel grade with high ductility, named as CP1000HD. It is an AHSS grade commonly used in the automotive industry for structural components. Its loading response was described using an elasto-plastic material model, combined with a ductile damage model for prediction of material failure. The elasto-plastic material behavior was calculated by an iterative radial return method using a Stiebler et al. [24] model, shown in Eq. (1), for defining the plastic response. The Stiebler model was calibrated by experimental data from hydraulic bulge testing according to IS0 16808 [25]. The experimental bulge data and the model fitting is shown in Fig. 2 and the Stiebler parameters c_1 to c_4 are shown in Table 1 and a Young's modulus of 210 GPa was assumed. The tensile mechanical properties of the material are presented in Table 2.

$$\hat{\sigma}(\varepsilon_p) = c_1 + c_2 \cdot \varepsilon_p + c_3 \cdot (1 - e^{c_4 \cdot \varepsilon_p}) \tag{1}$$

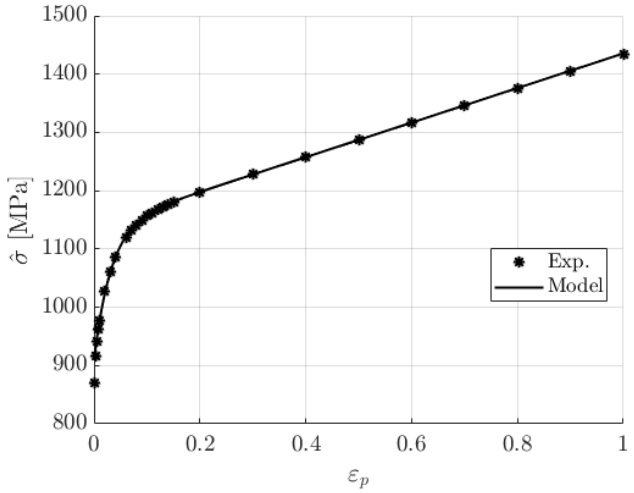

Fig. 2: Plastic hardening response from hydraulic bulge experiment and the fitted Stiebler plasticity model.

Table 1: Stiebler plasticity model parameters after curve fitting to experimental hydraulic bulge testing.

c_1 [MPa]	c_2 [MPa]	c_3 [MPa]	c_4
909.5	296.6	229.3	31.1

Table 2: Tensile mechanical properties of the CP1000HD grade, stating the rolling direction (RD), yield strength (Rp02), tensile strength (Rm), uniform elongation (Ag), total elongation (A80), n-value (nAg), r-value (r) and fracture toughness measured by the essential work of fracture method (EWF) transverse to RD.

RD	Rp02 [MPa]	Rm [MPa]	Ag [%]	A80 [%]	nAg	r	EWF [kJ/m^2]
0°	893	1052	7.3	11.1	0.071	0.91	-
45°	905	1052	7.0	10.6	0.068	1.02	-
90°	909	1062	7.1	10.7	0.068	0.96	282

The damage- and failure modelling implemented in the PFEM scheme was based on the Generalized Incremental Stress State Dependent Damage Model (GISSMO), developed by Neukamm et al. [26] and provides a stress-state dependent damage- and failure behavior. The stress-state was defined by the stress triaxiality η and Lode angle parameter $\bar{\theta}$, expressed in Eq. (2) and Eq. (3) respectively, where $\boldsymbol{\sigma}$ is the Cauchy stress tensor and $\boldsymbol{s}$ is the deviatoric stress tensor.

$$\eta = \frac{\mathrm{tr}(\boldsymbol{\sigma})}{3\sqrt{\frac{3}{2}\,\boldsymbol{s}:\boldsymbol{s}}} \tag{2}$$

$$\bar{\theta} = \frac{1}{3}\arccos\left(\frac{3\sqrt{3}}{2}\frac{det(\boldsymbol{s})}{\left(\frac{1}{2}\,\boldsymbol{s}:\boldsymbol{s}\right)^{\frac{3}{2}}}\right) \tag{3}$$

The damage- and failure model accumulates a damage parameter D according to Eq. (4), where n is the rate of damage accumulation, $\varepsilon_f(\eta,\bar{\theta})$ is the effective plastic failure strain, and $\dot{\varepsilon_p}$ is the effective plastic strain increment.

$$\dot{D} = \frac{n}{\varepsilon_f(\eta,\bar{\theta})} D^{\left(1-\frac{1}{n}\right)} \dot{\varepsilon_p} \tag{4}$$

Similarly, an instability parameter F accumulates according to Eq. (5), where $e_i(\eta)$ is the effective plastic instability strain and m is the material degradation rate.

$$\dot{F} = \frac{m}{\varepsilon_i(\eta)} F^{\left(1-\frac{1}{m}\right)} \dot{\varepsilon_p} \tag{5}$$

When $F = 1$, damage coupling to the stress tensor is activated to account for the loss of load bearing capacity due to void growth. This reduction of material strength is common in ductile metals, such as CP1000HD or similar AHSS grades. The damage related coupling to the load bearing capacity is defined according to Eq. (6), where D_c is the accumulated value of D when $F = 1$.

$$\tilde{\sigma} = \sigma\left(1-\widetilde{D}\right) \text{ where } \widetilde{D} = \left(\frac{D-D_c}{1-D_c}\right)^m \tag{6}$$

When the damage parameter D reaches a critical threshold value of $D = 0.99$, the stiffness of the element is lost, and the element is removed from the post-processing for clearer visualization of the material failure.

Experimental values of effective plastic failure strain were obtained using Digital Image Correlation (DIC) according to the work by [27]. This method extracted the strain field with a square 0.1 mm grids continuously during tensile testing of various tensile specimen and the effective plastic failure strain and the corresponding stress-state was calculated for each specimen. The specimens were designed to deform and failed at designated stress-states, thus cover a wide range of stress-states. This procedure enabled calibration of a failure locus, providing $\varepsilon_f(\eta,\bar{\theta})$ for the complete stress-state space. In this work, the Modified Mohr-Coulomb (MMC) locus developed by [28,29] was calibrated due to its renowned accuracy in failure modelling of ductile AHSS grades. Eq. (7) states the MMC equation, reduced to von Mises plasticity, where parameters C_1 to C_3 were calibrated with a least-squares fitting to the experimentally obtained values of the stress-state dependent effective plastic failure strains.

$$\varepsilon_f(\eta,\bar{\theta}) = \left(C_2 \left(\sqrt{\frac{1+C_1^2}{3}} \cos\left(\frac{\bar{\theta}\pi}{6}\right) + C_1\left(\eta + \frac{1}{3}\sin\left(\frac{\bar{\theta}\pi}{6}\right)\right)\right)\right)^{-\frac{1}{C_3}} \tag{7}$$

Eq. (8) relates the Lode angle parameter $\bar{\theta}$ to the stress triaxiality for plane stress assumption, which is considered during the tensile testing of the thin tensile specimen. Table 3 states the values of the calibrated parameters C_1 to C_3 for the CP1000HD MMC failure locus.

$$\bar{\theta} = 1 - \frac{2}{\pi}\cos^{-1}\left(-\frac{27}{2}\eta\left(\eta^2 - \frac{1}{3}\right)\right) \tag{8}$$

Table 3: Calibrated MMC parameters for the CP1000HD material.

C_1	C_2	C_3
0.1103	1.7166	0.4003

A critical topic of using such local phenomenological damage- and failure models is the mesh size dependency effects. As the experimental values of the effective plastic failure strains were determined using DIC facets of 0.1 mm, the values of $\varepsilon_f(\eta, \bar{\theta})$ were only valid for such element size. Smaller elements than the nominal 0.1 mm could reach the failure strain values in localized zones earlier in the deformation event than the nominal sized elements, thus failure would be prematurely predicted. To overcome this mesh size implications, mesh regularization according to [30] was applied. The mesh regularization technique scales the failure strain values according to the element size such that the failure behavior matches for all element sizes. The regularization factors were determined iteratively on a small-scale model subjected to simple shear.

Axisymmetric PFEM punching model

The axisymmetric PFEM model is schematically shown in Fig. 3, where the tools (dark grey) and blank (grey) are shown, along with the symmetry axis and the cutting clearance.

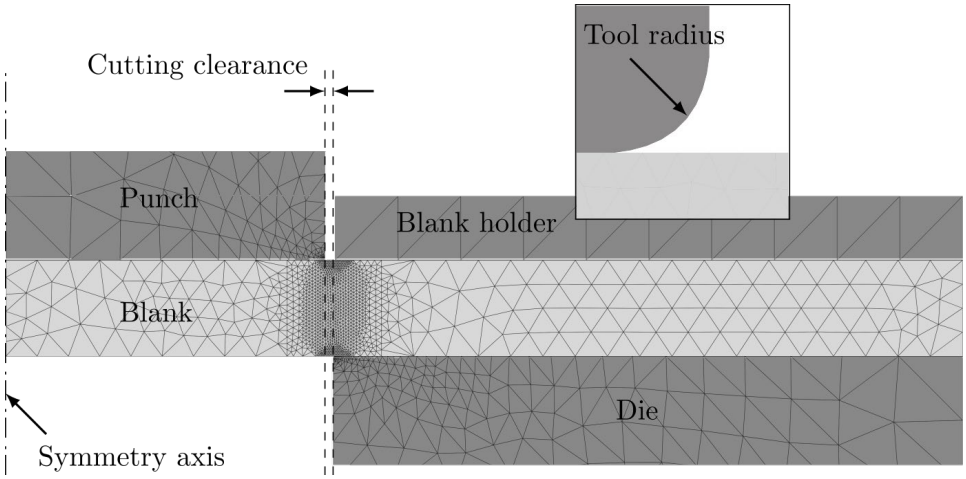

Fig. 3: Schematic overview of the axisymmetric PFEM model.

Small strain elasticity was applied to the tool parts, while the blank was assigned the elasto-plastic material model combined with the ductile damage model. A mixed displacement-pressure formulation was applied to the blank for avoiding volume locking issues that otherwise can occur using triangular elements with a single Gauss point. The mixed displacement theory was based on the work by Rodriguez et al. [18].

The process parameters of the various load cases are stated in Table 4, where the cutting die diameter was changed to vary the cutting clearance. As seen in Table 4, the tool edge radii were assumed to be circular with a radius of 30 μm, which represents sharp cutting tools. Laboratory punching experiments using the same clearances as in Table 4 were conducted with punching speeds of 0.05-2 mm/s which can be estimated as quasi-static conditions. The punching experiments were conducted using a servo-hydraulic clinching machine equipped with a dedicated

ISO 16630 HET tool according to [31]. The low cutting speeds justifies the lack of strain rate dependency in the PFEM shear cutting model.

Table 4: Process parameters for experimental and numerical punching configurations, showing the punch diameter (D_{Punch}), die diameter (D_{Die}), punch edge radius ($R_{Punch,edge}$), die edge radius ($R_{Die,edge}$) and blank thickness (T_{Blank}).

Clearance [%]	D_{Punch} [mm]	D_{Die} [mm]	$R_{Punch,edge}$ [µm]	$R_{Die,edge}$ [µm]	T_{Blank} [mm]
5.3	9.996	10.155	30	30	1.5
12.1	9.996	10.360	30	30	1.5
20.5	9.996	10.612	30	30	1.5
27.0	9.996	10.806	30	30	1.5

Results and discussion

The results from the different experimental and numerical hole punching configurations shown in Table 4 are presented in Fig. 4. It compares the distribution of each cut edge parameter (Roll-over, Burnish, Fracture and Burr) over the range of cutting clearances, 5.3%-27.0%, and the error bars in Fig. 4 presents the circumferential variation of the experimental cut edge parameters. The validation results shows that the PFEM numerical modelling can with good accuracy predict the experimental cut edge morphology. The numerical model can predict the appearance of burr at 27.0% cutting clearance, which according to Larour et al. [12] was proven as detrimental to edge formability. The results shows that the axisymmetric assumption was well justified for 12.1% and 20.5% cutting clearance, while a significant circumferential variation for 5.3% cutting clearance and a partial burr formation for 27.0% cutting clearance need 3D capabilities to be modelled exactly. However, this will increase the simulation time tremendously.

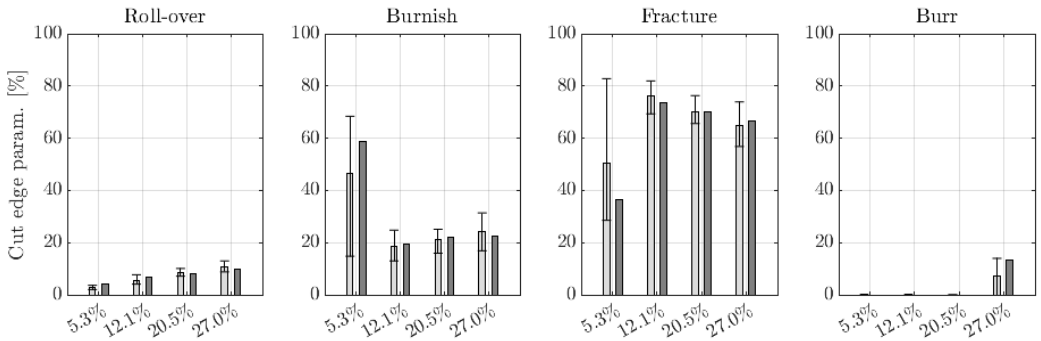

Fig. 4: Experimental (light grey) and numerical (dark grey) hole punching results in terms of cut edge parameters for the range of cutting clearances.

For 5.3% cutting clearance, the formation of secondary burnish was distinguished, as presented by Fig. 5 b). Here, the mismatching fracture angles α_{Punch} and β_{Die} cause the secondary burnish formation, as the cracks appearing at punch and could not be connected. However, the complex loading conditions of the secondary burnish formation, with bending and sudden change of fracture angle caused convergence issues using the implicit PFEM scheme. Therefore, the numerical modelling of the entire punching process of 5.3% was not able to finalize, but the fracture pattern of Fig. 5 b) manifests the formation of a secondary burnish surface. The cut edge parameters of Fig. 4 for 5.3% cutting clearance were furthermore based on the geometric markers of Fig. 5 b). Concludingly, further development of the PFEM implementation should incorporate explicit- or implicit dynamic schemes that can handle secondary burnish formation in a more computationally stable matter.

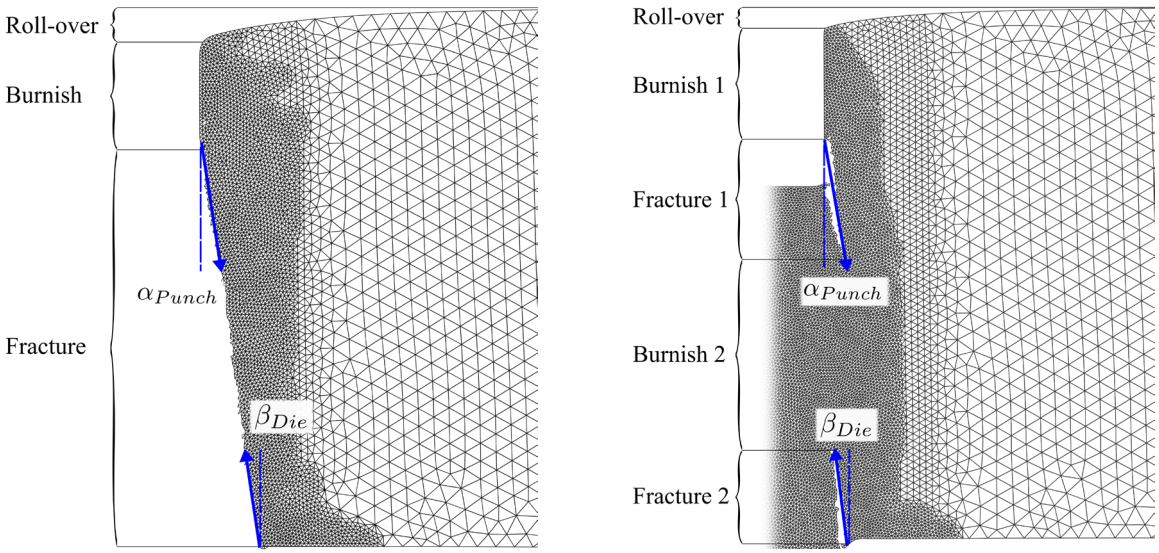

Fig. 5: Cut edges a) 12.1% cutting clearance and for b) 5.3% cutting clearance. a) shows the final cut edge where the ordinary cut edge shapes of roll-over, burnish and fracture were distinguished. Here the matching fracture angles ($\boldsymbol{\alpha_{Punch}}$, $\boldsymbol{\beta_{Die}}$) creates a uniform fracture surface. Meanwhile b) shows the mismatching fracture angles ($\boldsymbol{\alpha_{Punch}}$, $\boldsymbol{\beta_{Die}}$) and the corresponding secondary burnish formation. The length of the secondary burnish surface is estimated from the length of Burnish 2.

Conclusions

Based on the comparison between experimental and numerical shear cutting results, following conclusions are drawn:

- The presented PFEM shear cutting model is an accurate numerical tool for predicting the cut edge morphology over a large range of cutting clearances. The PFEM scheme ensures that element aspect ratios are kept adequate, and the ductile damage modelling enables modelling of the fracture process.
- By predicting the appearance of both secondary burnish (small clearance) and burr (large clearance), the PFEM model is useful for determining the feasible cutting clearance range for the AHSS grade investigated.
- The good correlation between experimental and numerical cut edge morphologies indicates that the residual cut edge results are useful for subsequent analysis of edge forming of fatigue.
- Given the circumferential variations of the experimental cut edge results it is suggested to investigate 3D PFEM shear cutting analysis. Such approach could further enhance modelling of subsequent forming- or fatigue analyses.

References

[1] A. Konieczny, T. Henderson, On formability limitations in stamping involving sheared edge stretching, SAE Technical Papers (2007). https://doi.org/10.4271/2007-01-0340

[2] H.C. Shih, C. Chiriac, M.F. Shi, The effects of AHSS shear edge conditions on edge fracture, ASME 2010 International Manufacturing Science and Engineering Conference, MSEC 2010 1 (2010) 599–608. https://doi.org/10.1115/MSEC2010-34062

[3] J. Dykeman, S. Malcolm, B. Yan, J. Chintamani, G. Huang, N. Ramisetti, H. Zhu, Characterization of edge fracture in various types of advanced high strength steel, SAE Technical Papers (2011). https://doi.org/10.4271/2011-01-1058

[4] D.J. Thomas, Understanding the effects of mechanical and laser cut-edges to prevent formability ruptures during automotive manufacturing, Journal of Failure Analysis and Prevention 13 (2013) 451–462. https://doi.org/10.1007/s11668-013-9696-z

[5] D. Frómeta, M. Tedesco, J. Calvo, A. Lara, S. Molas, D. Casellas, Assessing edge cracking resistance in AHSS automotive parts by the Essential Work of Fracture methodology, J Phys Conf Ser 896 (2017). https://doi.org/10.1088/1742-6596/896/1/012102

[6] A. Lara, I. Picas, D. Casellas, Effect of the cutting process on the fatigue behaviour of press hardened and high strength dual phase steels, J Mater Process Technol 213 (2013) 1908–1919. https://doi.org/10.1016/j.jmatprotec.2013.05.003

[7] I. Paetzold, F. Dittmann, M. Feistle, R. Golle, P. Haefele, H. Hoffmann, W. Volk, Influence of shear cutting parameters on the fatigue behavior of a dual-phase steel, J Phys Conf Ser 896 (2017). https://doi.org/10.1088/1742-6596/896/1/012107

[8] J. Stahl, I. Pätzold, R. Golle, C. Sunderkötter, H. Sieurin, W. Volk, Effect of one- And two-stage shear cutting on the fatigue strength of truck frame parts, Journal of Manufacturing and Materials Processing 4 (2020). https://doi.org/10.3390/JMMP4020052

[9] T. Shiozaki, Y. Tamai, T. Urabe, Effect of residual stresses on fatigue strength of high strength steel sheets with punched holes, Int J Fatigue 80 (2015) 324–331. https://doi.org/10.1016/J.IJFATIGUE.2015.06.018

[10] S. Parareda, D. Fr, D. Casellas, H. Sieurin, A. Mateo, Understanding the Fatigue Notch Sensitivity of High-Strength Steels through Fracture Toughness, Metals (Basel) 13 (2023) 1117. https://doi.org/https://doi.org/ 10.3390/met13061117

[11] D. Gustafsson, S. Parareda, L. Ortiz-Membrado, A. Mateo, E. Jiménez-Piqué, E. Olsson, Simulation of metal punching and trimming using minimal experimental characterization, J Mater Process Technol 321 (2023) 118148. https://doi.org/10.1016/j.jmatprotec.2023.118148

[12] P. Larour, J. Hinterdorfer, L. Wagner, J. Freudenthaler, A. Grünsteidl, M. Kerschbaum, Stretch flangeability of AHSS automotive grades versus cutting tool clearance, wear, angle and radial strain gradients, IOP Conf Ser Mater Sci Eng 1238 (2022) 012041. https://doi.org/10.1088/1757-899X/1238/1/012041

[13] O. Sandin, J.M.R. Prieto, S. Hammarberg, D. Casellas, Numerical modelling of shear cutting using particle methods, IOP Conf Ser Mater Sci Eng 1284 (2023) 012048. https://doi.org/10.1088/1757-899x/1284/1/012048

[14] X. Ye, J. Manuel, R. Prieto, R. Müller, An Improved Particle Finite Element Method for the Simulation of Machining Processes, 89 (2020) 13:1-13:0. https://doi.org/10.4230/OASIcs.iPMVM.2020.13

[15] J.M. Rodríguez, J.M. Carbonell, J.C. Cante, J. Oliver, Continuous chip formation in metal cutting processes using the Particle Finite Element Method (PFEM), Int J Solids Struct 120 (2017) 81–102. https://doi.org/10.1016/j.ijsolstr.2017.04.030

[16] E. Oñate, A. Franci, J.M. Carbonell, A particle finite element method for analysis of industrial forming processes, Comput Mech 54 (2014) 85–107. https://doi.org/10.1007/S00466-014-1016-2

[17] S.R. Idelsohn, E. Onate, F. Del Pin, The particle finite element method: A powerful tool to solve incompressible flows with free-surfaces and breaking waves, Int J Numer Methods Eng 61 (2004) 964–989. https://doi.org/10.1002/nme.1096

[18] J.M. Rodriguez, J.M. Carbonell, J.C. Cante, J. Oliver, The particle finite element method (PFEM) in thermo-mechanical problems, Int J Numer Methods Eng 107 (2016) 733–785. https://doi.org/10.1002/NME.5186

[19] Juan Manuel Rodriguez Prieto, Numerical modeling of metal cutting processes using the Particle Finite Element Method, (2013) 185.

[20] J.M. Rodriguez, S. Larsson, J.M. Carbonell, P. Jonsén, Implicit or explicit time integration schemes in the PFEM modeling of metal cutting processes, Comput Part Mech 9 (2022) 709–733. https://doi.org/10.1007/s40571-021-00439-5

[21] J.M. Rodriguez Prieto, J.M. Carbonell, J.C. Cante, J. Oliver, P. Jonsén, Generation of segmental chips in metal cutting modeled with the PFEM, Comput Mech 61 (2018) 639–655. https://doi.org/10.1007/s00466-017-1442-z

[22] E. Oñate, S.R. Idelsohn, F. Del Pin, R. Aubry, the Particle Finite Element Method — an Overview, Int J Comput Methods 01 (2004) 267–307. https://doi.org/10.1142/s0219876204000204

[23] J.R. Shewchuk, Condition guaranteeing the existence of higher-dimensional constrained Delaunay triangulations, in: Proceedings of the Annual Symposium on Computational Geometry, Minneapolis, MN, 1998: pp. 76–85. https://doi.org/10.1145/276884.276893

[24] K. Stiebler, H.D. Kunze, E. El-Magd, Description of the flow behaviour of a high strength austenitic steel under biaxial loading by a constitutive equation, Nuclear Engineering and Design 127 (1991) 85–93. https://doi.org/10.1016/0029-5493(91)90041-F

[25] ISO 16808:2014, Metallic materials — Sheet and strip — Determination of biaxial stress-strain curve by means of bulge test with optical measuring systems, (2014).

[26] F. Neukamm, M. Feucht, A. Haufe, K. Roll, On Closing the Constitutive Gap Between Forming and Crash Simulation, in: 10th International LS-DYNA Users Conference, 2008: pp. 12–21.

[27] T. Sjöberg, S. Marth, J. Kajberg, H.-A. Häggblad, Experimental characterisation of the evolution of triaxiality stress state for sheet metal materials, European Journal of Mechanics, A/Solids 66 (2017) 279–286. https://doi.org/10.1016/j.euromechsol.2017.07.013

[28] Y. Bai, X. Teng, T. Wierzbicki, On the application of stress triaxiality formula for plane strain fracture testing, Journal of Engineering Materials and Technology, Transactions of the ASME 131 (2009) 0210021–02100210. https://doi.org/10.1115/1.3078390

[29] Y. Bai, T. Wierzbicki, Application of extended Mohr-Coulomb criterion to ductile fracture, Int J Fract 161 (2010) 1–20. https://doi.org/10.1007/s10704-009-9422-8

[30] F. Andrade, M. Feucht, A. Haufe, F. Neukamm, An incremental stress state dependent damage model for ductile failure prediction, Int J Fract 200 (2016) 127–150. https://doi.org/10.1007/s10704-016-0081-2

[31] ISO 16630:2017, Metallic materials — Sheet and strip — Hole expanding test, International Standard Second Edi (2017).